4-D Reconstruction With Respiratory Correction for Gated Myocardial Perfusion SPECT

Wenyuan Qi, Yongyi Yang,* Chao Song, Miles N. Wernick, P. Hendrik Pretorius, and Michael A. King

Abstract—**Cardiac single photon emission computed tomography (SPECT) images are known to suffer from both cardiac and respiratory motion blur. In this paper, we investigate a 4-D reconstruction approach to suppress the effect of respiratory motion in gated cardiac SPECT imaging. In this approach, the sequence of cardiac gated images is reconstructed with respect to a reference respiratory amplitude bin in the respiratory cycle. To combat the challenge of inherent high-imaging noise, we utilize the data counts acquired during the entire respiratory cycle by making use of a motion-compensated scheme, in which both cardiac motion and respiratory motion are taken into account. In the experiments, we first use Monte Carlo simulated imaging data, wherein the ground truth is known for quantitative comparison. We then demonstrate the proposed approach on eight sets of clinical acquisitions, in which the subjects exhibit different degrees of respiratory motion blur. The quantitative evaluation results show that the 4-D reconstruction with respiratory correction could effectively reduce the effect of motion blur and lead to a more accurate reconstruction of the myocardium. The mean-squared error of the myocardium is reduced by 22%, and the left ventricle (LV) resolution is improved by 21%. Such improvement is also demonstrated with the clinical acquisitions, where the motion blur is markedly improved in the reconstructed LV wall and blood pool. The proposed approach is also noted to be effective on correcting the spill-over effect in the myocardium from nearby bowel or liver activities.**

Index Terms—**Cardiac SPECT, respiratory binning, cardiac gating, 4D reconstruction.**

I. INTRODUCTION

SINGLE photon emission computed tomography (SPECT) is a valuable, widely used tool for myocardial perfusion imaging in diagnosis of coronary artery diseases. To account for the effect of cardiac motion [1], cardiac gated SPECT is often used, which can provide additional important diagnostic information including ejection fraction, wall motion and wall thickening [2]. In gated SPECT, the data acquisition is divided into several time intervals of the cardiac cycle according to the ECG signal, and individual images are reconstructed for these intervals (aka gates).

While effective for depicting wall motion, gated SPECT images are known to suffer from significantly increased noise due to the much reduced data counts within the individual gate intervals. In the literature there have been many efforts aimed to improve the quality of gated images by using spatiotemporal processing techniques (collectively known as 4D methods). To name a few, a post-reconstruction spatiotemporal filter was used in [3]. In [4], a spatiotemporal regularization approach was introduced for reconstruction, where a prior motion model was used for temporal regularization. In [5], the image motion used in temporal regularization was estimated simultaneously along with the images during reconstruction. In [6] a motion-compensated 4D reconstruction approach was developed, and was demonstrated to significantly improve the reconstruction accuracy in gated SPECT [7], [8]; this approach was also demonstrated to be robust when the imaging dose was reduced in SPECT [9].

Aside from cardiac motion, SPECT images also suffer from artifacts caused by respiratory motion. This could lead to inaccuracies in both functional analyses of the left ventricle (LV) and regional myocardial perfusion [10]. Toward reducing the effect of respiratory motion, there also have been several approaches studied in cardiac SPECT imaging. For example, in [11] and [12], motion correction was first applied to the projection data prior to image reconstruction. A popular alternative approach is to use respiratory binned imaging, e.g., [10], [13], wherein the data acquisition is performed for different portions of the respiratory cycle during which the motion extent of the heart and diaphragm is reduced [10], [14]. Respiratory binning can be achieved either by phase gating, which is based on the relative temporal position within the respiratory cycle, or by amplitude binning, which is based on the respiratory magnitude measured from an external tracking device [15]. As with cardiac gating, respiratory binned SPECT also suffers from increased noise. To deal with this issue, one approach was to first estimate the respiratory motion from the reconstructed individual respiratory bins, and then correct for the respiratory motion in the reconstructed images [16]–[18]. In [19], a joint image-reconstruction approach was developed, in which the data acquired in individual respiratory bins were used collectively for reconstruction of the source distribution through motion compensation.

W. Qi, C. Song, and M. N. Wernick are with the Medical Imaging Research Center, Department of Electrical and Computer Engineering, Illinois Institute of Technology, Chicago, IL 60616 USA.

*Y. Yang is with the Medical Imaging Research Center, Department of Electrical and Computer Engineering, Illinois Institute of Technology, Chicago, IL 60616 USA.

P. H. Pretorius and M. A. King are with the Department of Radiology, Division of Nuclear Medicine, University of Massachusetts Medical School, Worcester, MA 01655 USA.

In SPECT imaging, cardiac gating and respiratory binning have been studied separately in the literature. This is largely due to the challenge associated with the much reduced data counts in individual cardiac gates or respiratory bins. Ideally, to correct for both cardiac and respiratory motion, one needs to employ both gating/binning schemes simultaneously. In [20], both cardiac contraction and respiratory motion correction were taken into account in clinical myocardial perfusion imaging, wherein respiratory motion correction was first applied to the acquired projection data prior to image reconstruction, and cardiac contraction correction was applied on reconstructed images subsequently to yield one perfusion image. In [21], end-expiration respiratory gating was used together with cardiac gating in a stationary SPECT system, in which only one respiratory phase was reconstructed (in order to reduce the respiratory motion blur) while other phases were rejected. However, in a conventional SPECT system where a rotating camera is used, such an approach would suffer from extremely high noise (as to be seen later in the experiments in Section III).

In this work, we develop a reconstruction approach to combat the effect of respiratory motion in cardiac gated SPECT. Our goal is to obtain a cardiac gated sequence from acquisitions with a conventional SPECT system while suppressing the effect of respiratory blur. For this purpose, we make use of both cardiac gating and respiratory binning in data acquisition. To combat the challenge associated with the much reduced data counts in individual respiratory-cardiac bins, we make use of our motion-compensated reconstruction schemes developed previously in cardiac gated reconstruction [7] and in respiratory binned SPECT [19]. We note that this work is based on our preliminary study in [22], where dual cardiac-respiratory corrected reconstruction was demonstrated to be feasible with simulated data. Encouraged by this initial success, in this study we fully develop and evaluate a reconstruction approach by considering its impact on the reconstructed LV wall, and furthermore, demonstrate the applicability of this approach on a number of clinical acquisitions where the subjects exhibit various levels of respiratory motion.

We note that dual gating has been studied for correction of respiratory motion in other modalities such as PET or PET/CT [23]–[26]. For example, in [27], both cardiac and respiratory gating was used in cardiac PET imaging and was found to improve the anatomical details of the heart in reconstruction. In [28], motion compensation during reconstruction was demonstrated to yield improved performance over post-reconstruction filtering in dual gated 4D cardiac PET imaging. In [29] and [30], respiratory and cardiac gated perfusion imaging was demonstrated to improve image resolution, contrast, and contrast-to-noise ratio in clinical PET images.

However, to the best of our knowledge, the reconstruction from cardiac-respiratory binned acquisitions has not been previously exploited in SPECT, largely due to several challenging aspects associated with conventional cardiac SPECT. Aside from the low data counts cited above, with a conventional SPECT system, the projection data are acquired at only two or three angles (depending on the SPECT system configuration) at a time. As a consequence, the effect of motion blur may vary among the acquired angles because of changes in respiratory patterns during the course of imaging. Compared to PET, the spatial resolution in SPECT is also more limited. To accommodate these, the proposed algorithm in this work is substantially different from that developed for dual-gated PET reconstruction. For example, in [28], both respiratory motion and cardiac motion were directly incorporated into the likelihood function, whereas in our proposed approach we use the cardiac motion as a temporal smoothing prior. The latter approach is expected to be more resilient to potential errors associated with motion estimation due to the high noise in SPECT, as the effect of temporal smoothing can be easily adjusted through the regularization parameter in the prior (Section II.B). The proposed approach is also noted to be different from [17], where respiratory correction was applied for ungated SPECT perfusion images.

The rest of the paper is organized as follows. In Section II, we describe the imaging model in dual cardiac-respiratory binned SPECT, and present our 4D reconstruction scheme and implementation details. In Section III, we provide a description of the experiments and evaluation methods. Afterward, we present the evaluation results in Section IV and conclusions in Section V.

II. 4D CARDIAC-RESPIRATORY RECONSTRUCTION

A. Imaging Model and Problem Statement

In dual cardiac-respiratory binned imaging, the data acquisition is synchronized with both the electrocardiogram (ECG) signal and the respiratory cycles [23], [24]. Accordingly, the acquired data can be re-binned for different cardiac subintervals and respiratory magnitude intervals.

Mathematically, the data acquisition is described by the following linear model:

$$E[\mathbf{g}_{r,k}] = \mathbf{H}\mathbf{f}_{r,k} + \mathbf{s}_{r,k}, k = 1, ..., K, r = 1, ..., R \qquad (1)$$

where $\mathbf{g}_{r,k}$ and $\mathbf{f}_{r,k}$ are vectors representing the acquired data (sinogram) and source distribution, respectively, for respiratory bin r and cardiac gate k, $\mathbf{s}_{r,k}$ is the corresponding scatter component, K and R are the numbers of bins of the cardiac cycle and respiratory period, respectively. In (1), $\mathbf{H}$ is the system matrix describing the imaging process, and $E[\cdot]$ is the expectation operator. In $\mathbf{H}$, each element $h_{i,j}$ represents the probability that a photon emitted at voxel location j is detected at detector bin i without being scattered. In this study the depth dependent blur and attenuation effects are both incorporated into the system matrix $\mathbf{H}$ [31].

Our objective is to reconstruct a single cardiac gated sequence such that it depicts the cardiac wall motion while reducing the effect of respiratory blur. To accomplish this, one straightforward approach would be, as in [21], to reconstruct the images from data acquired only in a chosen reference respiratory bin $r = r_0$; this would effectively limit the extent of respiratory motion in the resulting sequence $\{\mathbf{f}_{r_0,k}, k = 1, ..., K\}$. However, such an approach would inevitably suffer from extremely high noise in the reconstruction (as to be seen later in the results in Section IV.E), because the acquired counts from the rest of respiratory bins are not utilized.

Alternatively, to alleviate the increased noise, one could rebin the data for each cardiac gate by combining counts from multiple respiratory bins, as in conventional cardiac gated SPECT; of course, this would lead to increased motion blur associated with the different respiratory bins. In this study, we propose a reconstruction approach, in which we aim to reconstruct a cardiac gated sequence with respect to a given reference respiratory magnitude bin while utilizing the data acquired from the entire respiratory cycle.

B. 4D Reconstruction for Single Respiratory Bin

To facilitate the development of the proposed reconstruction approach from all respiratory bins, below we first explain in concept how to apply 4D reconstruction from a single reference respiratory bin. Here we consider the 4D approach previously developed for cardiac-gated SPECT reconstruction [7]. Without loss of generality, let $r_0 = 1$ be the reference respiratory bin. Within this reference bin, the dual gated imaging model (1) is reduced to:

$$E[\mathbf{g}_{1,k}] = \mathbf{H}\mathbf{f}_{1,k} + \mathbf{s}_{1,k} \qquad (2)$$

Our goal is to reconstruct the cardiac gated sequence $\mathbf{f}_{1,k}, k = 1, ..., K$. Conceptually, this is equivalent to reconstruction in traditional cardiac gated SPECT where no respiratory gating is applied (except that the data counts now are much lower).

For convenience, let $\mathbf{G_1}$ denote the collection of acquired data over all the cardiac gates during the reference respiratory bin, i.e., $\mathbf{G_1} \equiv [\mathbf{g}_{1,1}, ..., \mathbf{g}_{1,K}]$. Similar, let $\mathbf{F_1} \equiv [\mathbf{f}_{1,1}, ..., \mathbf{f}_{1,K}]$, a vector denoting the corresponding cardiac gated sequence. Then with 4D reconstruction [7], we seek the solution via maximum *a posteriori* (MAP) estimation as

$$\hat{\mathbf{F}}_1 = \arg\max_{\mathbf{F}_1}\{\log p(\mathbf{G_1}|\mathbf{F_1}) + \log p(\mathbf{F_1})\} \qquad (3)$$

where $p(\mathbf{G_1}|\mathbf{F_1})$ is the likelihood function of $\mathbf{G_1}$ parameterized by $\mathbf{F_1}$, and $p(\mathbf{F_1})$ is a prior on $\mathbf{F_1}$ (as given below).

The prior term $p(\mathbf{F_1})$ in (3) is defined in the form of a separable Gibbs prior as follows [8]:

$$p(\mathbf{F_1}) \propto exp[-\beta_s U_s(\mathbf{F_1}) - \beta_t U_t(\mathbf{F_1})] \qquad (4)$$

where $U_s(\mathbf{F_1})$ is an energy term defined to enforce spatial smoothing within individual gates, $U_t(\mathbf{F_1})$ is an energy term to enforce smoothing along the motion trajectories across the different gates, β_s and β_t are their corresponding scalar weighting factors [7].

In (4) the energy function $U_t(\mathbf{F_1})$ is used to exploit the correlation of the image signal among the different cardiac gates. Specifically, it is defined as

$$U_t(\mathbf{F_1}) = \sum_{k=1}^{K}\left\| \mathbf{f}_{1,k} - \frac{1}{C}\sum_{l=1,l\neq k}^{K}\left[1 - \frac{2|k-l|}{K}\right]M_{l\to k}\mathbf{f}_{1,l} \right\|^2 \quad (5)$$

where $M_{l\to k}$ denotes the motion-compensated prediction operator from gate l to gate k, C is a normalization constant for the weighted temporal prediction to have unit DC gain, and $\| \cdot \|$ is the L^2 norm. The above definition is to penalize the difference in image intensity along the trajectories of a

given point. The weighting coefficients are so defined that temporally neighboring frames will have more contribution to the current frame than frames that are further away. The operator $M_{l\to k}$ in (5) depends on the cardiac motion from cardiac gate l to gate k [7].

C. 4D Reconstruction From All Respiratory Bins

The 4D reconstruction approach in (3) describes how to determine the cardiac gated sequence using acquisition from a single reference respiratory bin. Next, we expand this approach by also utilizing the acquired data from all other respiratory bins. Toward this goal, we employ a motion model to represent the different respiratory bins as a transformation of the reference respiratory bin $r_0 = 1$. This enables the acquired data to be described in terms of this reference bin. The cardiac gated images are then reconstructed with respect to this reference bin through statistical estimation.

Specifically, let the cardiac gated images $\mathbf{f}_{r,k}$ in respiratory bin $r, r = 2, ..., R$ be denoted with respect to the reference respiratory bin as:

$$\mathbf{f}_{r,k} = T_r\mathbf{f}_{1,k} \qquad (6)$$

where T_r is the motion operator between respiratory bin r and the reference bin. Then we can rewrite (1) as:

$$E[\mathbf{g}_{r,k}] = \mathbf{H}T_r\mathbf{f}_{1,k} + s_{r,k}, k = 1, ..., K, r = 1, ..., R \quad (7)$$

where T_1 is implicitly assumed to be the identify operator. Our goal is to reconstruct the cardiac gated sequence $\mathbf{f}_{1,k}, k = 1, ..., K$ from (7). We seek an estimation approach, in which we make use of all respiratory bins, as described as below.

Let $\mathbf{G}$ denote the collection of acquired data over all the respiratory bins and cardiac gates, i.e., $\mathbf{G} \equiv [\mathbf{g}_{1,1}, ..., \mathbf{g}_{R,1}, \mathbf{g}_{1,2}, ..., \mathbf{g}_{R,2}, ..., \mathbf{g}_{1,K}, ..., \mathbf{g}_{R,K}]$. Then we seek the solution for $\mathbf{F}_1$ from (7) via MAP estimation as

$$\hat{\mathbf{F}}_1 = \arg\max_{\mathbf{F}_1}\{\log p(\mathbf{G}|\mathbf{F}_1) + \log p(\mathbf{F}_1)\} \qquad (8)$$

where $p(\mathbf{G}|\mathbf{F}_1)$ is the likelihood function of $\mathbf{G}$ parameterized by $\mathbf{F}_1$, and $p(\mathbf{F}_1)$ is the same prior on $\mathbf{F}_1$ as in (4). Under the assumption of independence in the acquired data among the different respiratory bins and cardiac gates, the likelihood term $p(\mathbf{G}|\mathbf{F}_1)$ can be written in terms of the individual gates/bins as

$$\log p(\mathbf{G}|\mathbf{F}_1) = \sum_{r=1}^{R}\sum_{k=1}^{K}\log p(\mathbf{g}_{r,k}|\mathbf{f}_{1,k}) \qquad (9)$$

where the likelihood term $p(\mathbf{g}_{r,k}|\mathbf{f}_{1,k})$ is specified by the imaging model in (7).

We assume a Poisson likelihood function for the noise model in (1) for SPECT. With all the terms defined, the MAP estimation in (8) can then be solved by minimizing the following objective function:

$$\begin{aligned} J(\mathbf{F_1}) = \sum_{r=1}^{R}\sum_{k=1}^{K}\sum_{i=1}^{D}&\{\mathbf{H}T_r\mathbf{f}_{1,k}(i) + \mathbf{s}_{r,k}(i) \\ &- \mathbf{g}_{r,k}(i)\log[\mathbf{H}T_r\mathbf{f}_{1,k}(i) + \mathbf{s}_{r,k}(i)]\} \\ &+ \beta_s U_s(\mathbf{F_1}) + \beta_t U_t(\mathbf{F_1}) \qquad (10) \end{aligned}$$
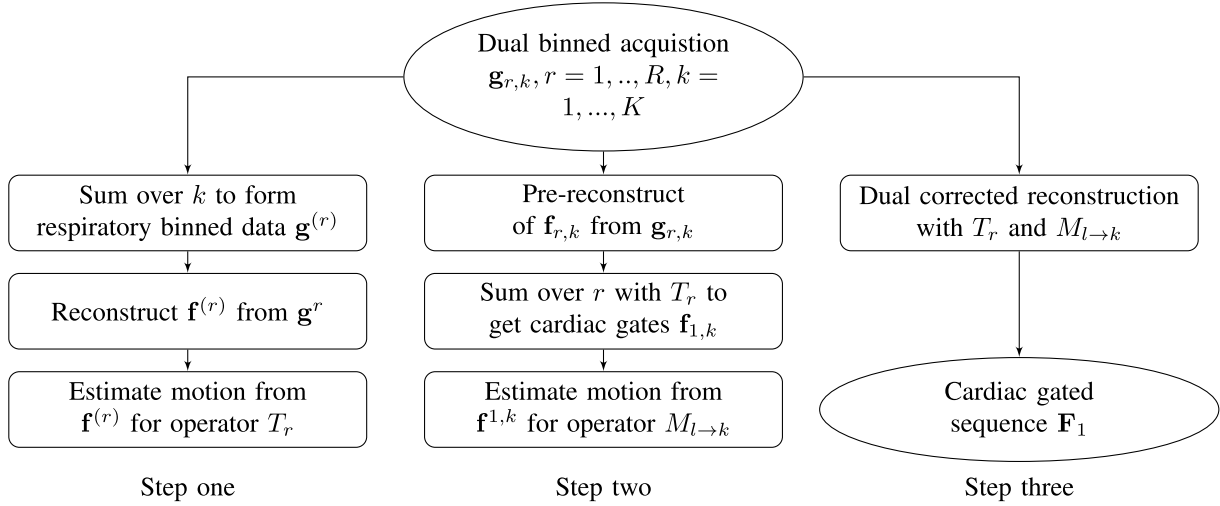
Fig. 1. Flow chart of proposed dual cardiac-respiratory binned reconstruction.

where $\mathbf{H}T_r\mathbf{f}_{1,k}(i), \mathbf{s}_{r,k}(i), \mathbf{g}_{r,k}(i)$ denote the i-th element of $\mathbf{H}T_r\mathbf{f}_{1,k}, \mathbf{s}_{r,k}, \mathbf{g}_{r,k}$, respectively, and D is the total number of detector bins.

In our experiments, the modified block sequential regularized expectation-maximization (BSREM) algorithm [32] was applied for the optimization problem in (10) as previously in cardiac gated 4D [8]. The modified BSREM algorithm is known to be globally convergent and typically faster than non-ordered-subset algorithms.

D. Implementation of Dual Cardiac-Respiratory Reconstruction

The objective function in (10) for 4D reconstruction involves both respiratory motion operator T_r and cardiac motion operator $M_{l\to k}$. In our implementation, we determine their associated motion information through a pre-reconstruction of the dual cardiac-respiratory binned data. Below we describe this procedure in three sequential steps.

Step 1: Respiratory Motion Estimation: In order to increase the data counts for each respiratory bin (thereby decreasing noise), the dual cardiac-respiratory binned acquisition is first collapsed over the cardiac cycle to get a sum for each respiratory bin r. Let $\mathbf{g}^{(r)}$ denote this sum. That is,

$$\mathbf{g}^{(r)} = \sum_{k=1}^{K} \mathbf{g}_{r,k}, \ r = 1, ..., R \tag{11}$$

Afterward, $\mathbf{g}^{(r)}$ is used to reconstruct the image for respiratory bin r, denoted by $\mathbf{f}^{(r)}, r = 1, ..., R$. The reconstructed $\mathbf{f}^{(r)}$ is then used to determine the image motion with respect to the reference bin $\mathbf{f}^{(r_0)}$. In our experiments, we used a translational model for the myocardium across the different respiratory bins. While simple, such a translational model was previously demonstrated to be effective for respiratory correction in cardiac SPECT owing to its limited resolution [18]. To determine the motion for $\mathbf{f}^{(r)}$, the myocardium was first segmented out based on the image intensity using a region growing method, and its center of gravity was used to determine the motion parameters.

Step 2: Cardiac Motion Estimation: To simplify the problem, in this study the image motion during a cardiac cycle is assumed to be constant among different respiratory bins. Based on this assumption, we first obtain an estimate for each cardiac gate by combining the data acquired from diffent respiratory bins. This is accomplished through the respiratory motion T_r determined in Step 1 above. Specifically, for each cardiac gate k, we first obtain an initial reconstruction of $\mathbf{f}_{r,k}$ from $\mathbf{g}_{r,k}, \ r = 1, ..., R$. The different respiratory bins are then combined (for noise suppression) to yield an estimate for each cardiac gate as:

$$\hat{\mathbf{f}}_{1,k} = \frac{1}{R} \sum_{r=1}^{R} T_r \mathbf{f}_{r,k} \tag{12}$$

Afterward, the images $\hat{\mathbf{f}}_{1,k}, k = 1, ..., K$ are used to determine the image motion across different cardiac gates. In our experiments, the optical flow method [33] was used to estimate the image motion as in [34]. The initial reconstruction of $\mathbf{f}_{r,k}$ was performed without temporal smoothing (i.e., $\beta_t = 0$ in (4)).

Step 3: 4D Reconstruction: With both the respiratory motion for T_r and cardiac motion for $M_{l\to k}$ determined above, the cardiac image sequence $\mathbf{F}_1$ is next determined though optimizing the objective function in (10). As a summary, the dual cardiac-respiratory reconstruction procedure is illustrated with a flow chart shown in Figure 1.

III. EXPERIMENTS AND EVALUATION STUDY

A. Imaging Datasets

For the purpose of quantitative evaluation, we first test the proposed reconstruction approach with simulated imaging data for which the ground truth is known. Afterward, we demonstrate the approach with several sets of clinical acquisitions, as described below.

1) Phantom Simulation: The 4D NURBS-based cardiac-torso (NCAT) 2.0 phantom [35] was used to simulate gated SPECT imaging with Tc-99m labeled sestamibi
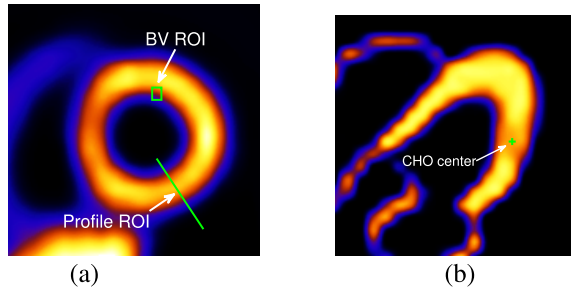
Fig. 2. Different ROIs used in numerical evaluation: (a) BV ROI is for regional bias-Std analysis, and Profile ROI is for quantifying the intensity profile of the LV, (b) CHO center indicates the center position of the introduced perfusion defect used in lesion detectablity evaluation.

as the imaging agent. The simulation was based on a Philips Prism 3000 SPECT system with a low-energy high-resolution (LEHR) collimator. The projection data were 64×64 bins with a pixel size of 0.634 cm. For a circular camera rotation of 28.5 cm radius, 64 angular projection sets were collected. The average spatial resolution at the location of the heart in the image slices was approximately 1.3 cm in full-width at half-maximum (FWHM).

In order to simulate the continuous nature of respiratory motion, 28 equally spaced intervals in magnitude were generated within the respiratory cycle. For each respiratory interval, 8 cardiac gates were simulated. Afterward, the 28 intervals were rebinned by summing every 4 intervals, leading to 7 respiratory intervals in the final projection data. The extent of diaphragm motion was 2 cm, and the extent of the anterior-posterior expansion of the chest was 1.2 cm. These parameters were set for normal breathing in the NCAT software. The corresponding motion of the heart was calculated as 1.59cm along the superior-inferior direction and 0.95cm along the anterior-posterior direction. The heart motion was rigid translation for the heart itself, but non-rigid with respect to the other organs in the chest [36]. The respiratory period and cardiac cycle were 5 sec and 1 sec, respectively.

The phantom was generated with the following body dimensions: 35.2cm, 26.7cm and 41.7cm in width, height and axial dimensions, respectively. Two datasets were generated, one with a perfusion defect and the other without. For the former, a transmural perfusion defect with 15% intensity reduction was introduced in the anterior-posterior region of the LV. The extent was 20 degrees in the circumferential dimension, and 6 voxels in height along the long-axis dimension. A transaxial slice with the defect was shown in Figure 2(b).

Monte-Carlo simulation with SIMIND [37] was used for the projection data. Poisson noise at a level of 8 million total counts was introduced for the entire acquisition as in a typical clinical acquisition. The following relative activity levels were introduced for the different organs: heart (ventricular and atrial walls) 1.0, liver 1.0, kidney 1.0, spleen 1.0, gall bladder 0.8, and tissue background 0.053. Attenuation, scatter and detector response effects were all included in the simulation data. In the reconstruction, both attenuation and detector depth-dependent blur effects were directly modeled in the system matrix in (1). For attenuation correction, we used the averaged attenuation map over all respiratory and cardiac gates.

The scatter component was estimated using the triple energy window (TEW) method [38] and included in the likelihood function. The photopeak window was 20% centered at 140 keV, and a 3.5 keV window abutted to the lower side of the photopeak window was used for scatter correction. A total of 30 noise realizations were used in our evaluation.

As reference for quantitative evaluation, the cardiac gated images in the reference respiratory bin were reconstructed from the simulated photopeak window projection data (depth dependent spatial resolution was included, but neither attenuation nor scatter) using the ordered subset expectation-maximization (OSEM) [39] algorithm (16 subsets, 10 iterations). These images represent the ideal scenario of perfect acquisition (denoted as "Ideal" below).

2) Clinical Data: As a preliminary demonstration, we also tested the proposed approach on eight sets of clinical data, which were acquired under IRB approval with informed content. The dataset was acquired in list-mode by a Philips BrightView SPECT/CT system with 64 projections over 180° and a 128×128 matrix. The pixel size was 0.467 cm. The acquisition started from right anterior oblique, passed through anterior and left anterior oblique, and ended at left lateral oblique. Events were recorded within a symmetric energy window centered on 140.5keV with a width of 15%. A scatter window was also acquired which was centered at 120keV with a 5% width. With patients quietly breathing, cone-beam CT imaging (60 seconds) was performed prior to emission and was used for the estimation of attenuation maps. A visual tracking system (Vicon Motion Systems, Inc., Lake forest, CA) was used to record the respiratory magnitude, based on which the acquired data were rebinned into seven respiratory magnitude bins [40]. In addition, eight cardiac gates were used according to the ECG signal. For reconstruction, the TEW method [38] was used for scatter correction.

Among the eight clinical data sets, there were seven male and one female, aged from 52 to 73 (56.6 ± 8.0). Also, seven were interpreted as having normal scans, and one (patient #2) with apical thinning or a small apical infarct. The acquired total counts ranged from 14 million to 18 million for the eight subjects. The peak-to-peak displacement motion magnitude values of the LV are 1.77 ± 0.55 cm among these patients, and the peak displacement values from the reference neutral position of the LV are 1.13 ± 0.35 cm. The peak-to-peak displacement was determined from the translational motion between two extreme bins in the respiratory amplitue.

B. Numerical Evaluation Metrics

1) Overall Error Level of Myocardium: To quantify the overall accuracy of the reconstructed myocardium, we computed the mean squared error (MSE) of the reconstructed images for a $30 \times 28 \times 20$ volumetric region containing the entire LV. The MSE of this volume of interest (VOI) was computed among all the cardiac gates within the cardiac cycle [8].

2) Regional Bias-Standard Deviation (std) Analyses: To quantify the regional accuracy of the reconstructed LV, we conducted bias-std analyses on a region of interest (ROI) selected

on the LV wall, as illustrated in Figure 2(a). Such analyses provided results on both the bias and std levels of the regional intensity of the LV wall in the reconstruction. In our experiments, a total of $Q = 30$ noise realizations were used [8].

3) LV Resolution: In order to examine the effect of different reconstruction schemes on the spatial resolution in the reconstructed images, we plotted the image intensity profile for a section across the LV wall, as shown in Figure 2(a). We then quantified the wall resolution by calculating the FWHM of this cross-section of the LV.

4) Lesion Detectability: To quantify lesion detectability in the reconstructed gated images, a channelized Hotelling observer (CHO) was used [41]. As in [31], the CHO was applied to end-diastole (ED) gate during which the heart wall is most expanded and small lesions are easier to be seen. In the CHO, four rotationally symmetric, non-overlapping input channels were used and internal noise was included as in [7]. In our experiments a total of 60 noise realizations (30 lesion-present and 30 lesion-absent) were used and the reconstructed images by each method were assessed by the CHO. The CHO ROI was show in Figure 2(b). The detection performance was summarized using the area under the receiver operating characteristic (ROC) curve (denoted as Az). These ROC studies represented a "signal-known exactly" and "background-known exactly" observer study.

All the metrics above were used for simulated phantom images. The LV resolution was also applied for the clinical images.

C. Reconstruction Methods for Comparison

For convenience, the proposed 4D reconstruction approach from dual cardiac-respiratory binned data was referred to as 4D-D. For the purpose of comparison, in the experiment we also considered the following methods for reconstructing the cardiac gated images: 1) 4D reconstruction with traditional cardiac gating (i.e., no respiratory correction was used; this method was denoted as 4D-C); 2) 4D reconstruction from combining two respiratory bins near the end-expiratory phase (denoted as 4D-R); 3) a clinical spatiotemporal processing method [31], in which the cardiac gated images were first reconstructed by filered-back projection (FBP), then processed spatially with a 3D Butterworth filter (order=2.4, cutoff frequency of 0.2 cycles/voxel) and temporally with a 3-point filter (impulse response 1/4, 2/4, 1/4); it was denoted as ST121.

IV. RESULTS AND DISCUSSIONS

A. Quantitative Accuracy of Reconstructed Myocardium

In Figure 3, we show the MSE results obtained by the proposed dual cardiac-respiratory 4D reconstruction algorithm 4D-D. The reconstructed image intensity represents the photon counts. Thus, the square root of MSE has the same units of photon counts. To demonstrate the effect of spatial and temporal smoothing, the parameters β_s and β_t in (4) were varied as follows: $\beta_s = 0$, 0.0001 and 0.0005, and $\beta_t = 0$, 0.0001, 0.0005, 0.001 and 0.005. Note that $\beta_s = 0$ corresponds to no spatial smoothing applied. Thus, the curve $\beta_s = 0$ in Figure 3 shows the effect of temporal smoothing alone as
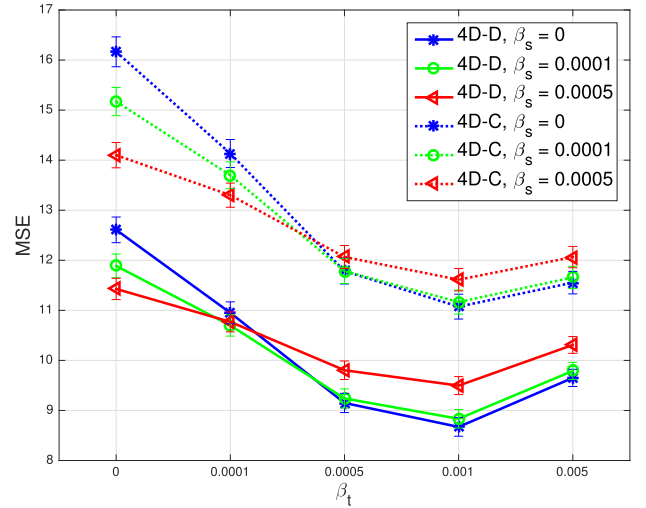

Fig. 3. MSE results of the reconstructed myocardium obtained with different reconstruction methods. 4D-D is the proposed dual cardiac-respiratory binned 4D reconstruction, and 4D-C is the traditional cardiac gated 4D reconstruction. Parameters β_s and β_t are used to control the level of spatial and temporal smoothing, respectively. These results were averaged from 30 noise realizations. The error bars indicate the standard deviation values.

β_t was successivly increased; in particular, the point $\beta_t = 0$ on this curve corresponds to neither spatial nor temporal smoothing applied. Similarly, the curves $\beta_s = 0.0001$ and $\beta_s = 0.0005$ show the results when spatial smoothing was applied in addition to temporal smoothing. These results were averaged from 30 noise realizations. The error bars represent the standard-deviation value at each point.

For comparison, the MSE results are also shown in Figure 3 for 4D-C, i.e., reconstruction with only cardiac gating.

From Figure 3, the MSE in 4D-D is noted to decrease as β_t increased from 0 to 0.001 for each β_s. The best MSE = 8.67 is obtained by $\beta_s = 0$ and $\beta_t = 0.001$, i.e., without any spatial smoothing. Moreover, when temporal smoothing β_t is small (0 and 0.0001), the MSE shows improvement with increased spatial smoothing; however, this improvement diminishes once temporal smoothing is increased. In comparison, similar behavior is also noted in the MSE results of 4D-C reconstruction, with the best MSE = 11.07 obtained also by $\beta_s = 0$ and $\beta_t = 0.001$. However, the MSE values in 4D-C are notably higher than that in 4D-D. These results demonstrate that using respiratory gating in 4D-D can lead to more accurate reconstruction of the myocardium than 4D-C.

B. LV Regional Accuracy

In Figure 4, we show the bias-std analysis results from 4D-D reconstruction. The ROI used was shown in Figure 2(a). To illustrate the effect of temporal smoothing, each curve in Figure 4 was obtained by varying $\beta_t = 0$, 0.0001, 0.0005, 0.001 and 0.005 while β_s was held constant. The curve $\beta_s = 0$ corresponds to no spatial smoothing. On each curve, the left-end point corresponds to $\beta_t = 0$, and the right-end point corresponds to $\beta_t = 0.005$. The bias and std values were obtained from 30 noise realizations.
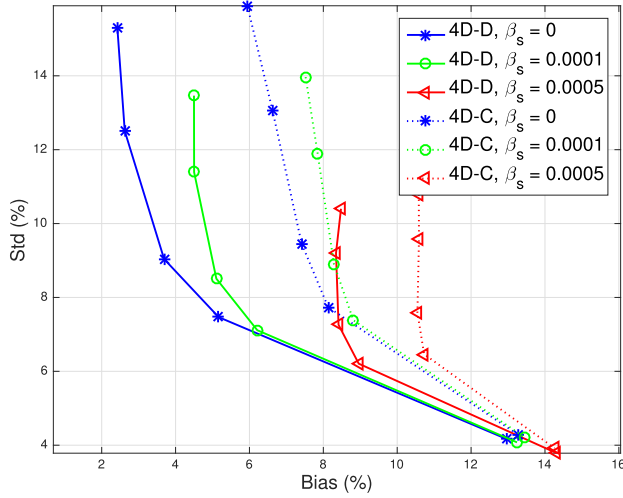
Fig. 4. Regional bias-std plots of the reconstructed LV. 4D-D is the proposed dual cardiac-respiratory binned 4D reconstruction, and 4D-C is the traditional cardiac gated 4D reconstruction. Each curve was obtained by varying the temporal smoothing parameter, with the left-end point corresponding to no temporal smoothing.

From Figure 4, it is noted that, as β_t increased from 0 to 0.005, each curve in 4D-D shows a decreasing trend in the noise level (std), but at the expense of increased bias. The use of spatial smoothing β_s can further reduce the noise level, but the bias level is notably increased. In contrast, with temporal smoothing the noise level can be reduced faster than the increase in bias. Consequently, at the same noise level, temporal smoothing could yield a smaller bias than spatial smoothing. This is the consistent with the observation above that the best MSE result was obtained when no spatial smoothing was applied.

For comparison, the bias-std results are also shown in Figure 4 for 4D-C, i.e., reconstruction with only cardiac gating.

As can be seen, the curves in 4D-C show similar trending behaviors as in 4D-D. While the std level is similar between the two, the bias level in each curve is notably higher in 4D-C than its counterpart in 4D-D. These results indicate that 4D-D reconstruction could improve the regional accuracy of the LV while without increasing the noise level, thanks to the use of respiratory motion correction.

C. Intensity Profile and LV Resolution

To demonstrate the effect on the resolution of the reconstructed LV wall, we show in Figure 5 the intensity profile obtained by 4D-D for a cross-section through the LV. This LV cross-section was shown in Figure 2. For comparison, the intensity profile is also shown for 4D-C reconstruction in Figure 5. These results were averaged from 30 noise realizations. The smoothing parameter for these curves are $\beta_s = 0$ and $\beta_t = 0.001$ (optimal MSE). As can be seen, the bias level in 4D-D was greatly reduced across the LV wall (particularly the middle section) compared to 4D-C. Moreover, with respiratory correction, the effective width of the LV in 4D-D is noted to be closer to that of
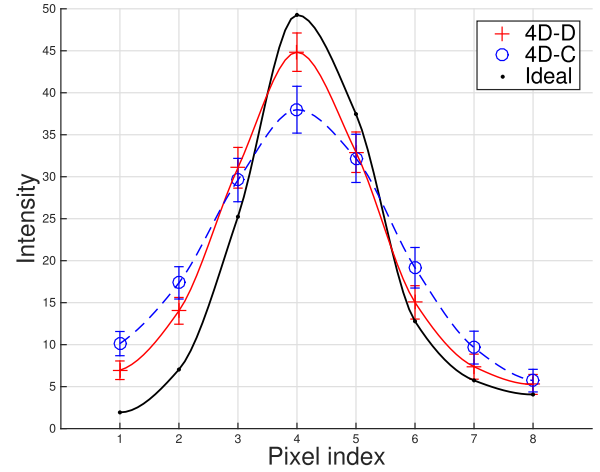

Fig. 5. Intensity profile of the reconstructed LV wall. 4D-D is the proposed dual cardiac-respiratory binned 4D reconstruction, and 4D-C is the traditional cardiac gated 4D reconstruction. These plots were from an average of 30 noise realizations.
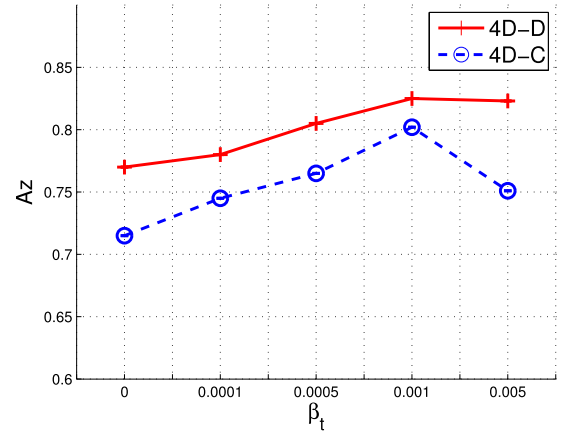

Fig. 6. Lesion detectability measured by CHO with different temporal smoothing ($\beta_s = 0$). 4D-D is the proposed dual cardiac-respiratory binned 4D reconstruction, and 4D-C is the traditional cardiac gated 4D reconstruction.

Ideal reference than in 4D-C. Quantitatively, the FWHM of 4D-D is 1.96±0.08 cm, compared to 2.48±0.19 cm for 4D-C. As reference, the FWHM of Ideal is 1.62 cm. In comparison, the LV resolution in 4D-D is improved by 21% over 4D-C, and its standard-deviation was also notably reduced.

D. Lesion Detectability

In Figure 6 we show the CHO results on lesion detectability obtained by 4D-D reconstruction. To illustrate the effect of temporal smoothing, we show the Az value obtained by varying $\beta_t = 0$, 0.0001, 0.0005, 0.001 and 0.005, while $\beta_s = 0$ (based on optimal MSE). For comparison, the results are also shown in Figure 6 for reconstruction with 4D-C. As can be seen, the 4D-D curve is higher than 4D-C over the range $\beta_t = 0$ to 0.005. In particular, the best Az = 0.82 was obtained by 4D-D with $\beta_t = 0.001$, compared to Az = 0.79 by 4D-C. Interestingly, this optimal setting also yielded the best MSE value above. Thus, respiratory correction in 4D-D reconstruction also improved the lesion detectability.
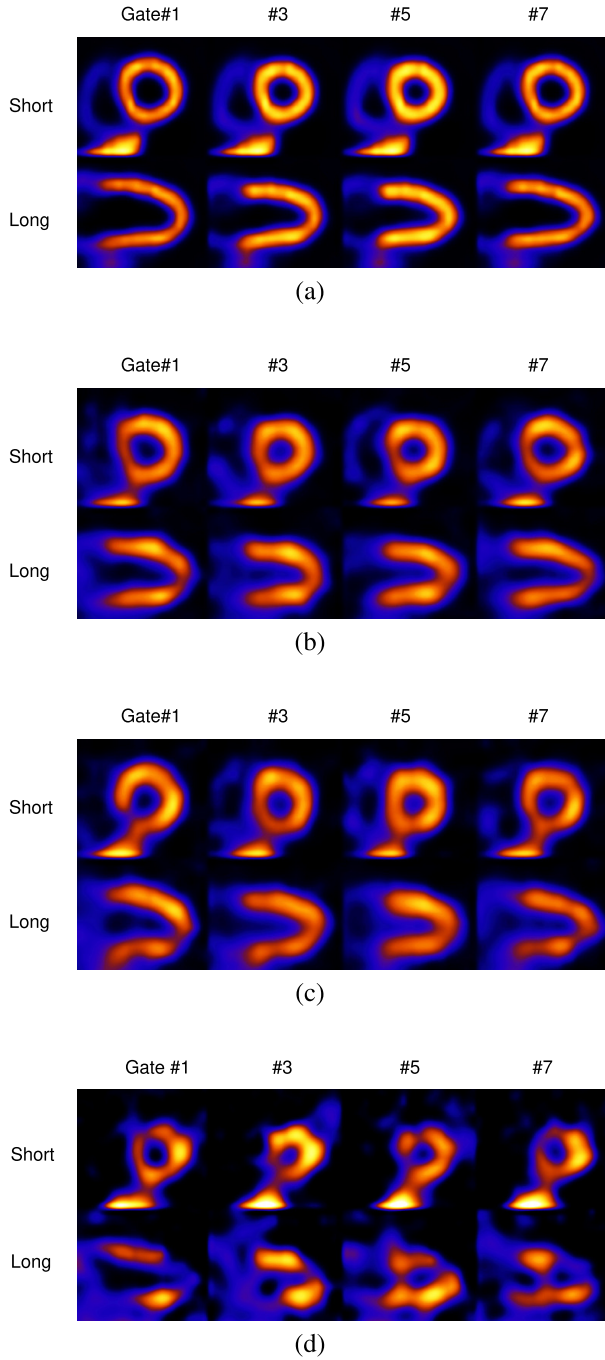
(a)

(b)

(c)

(d)

Fig. 7. Reconstructed short axis and vertical-long axis slices of NCAT by different methods: (a) Ideal reference, (b) proposed 4D reconstruction with dual cardiac-respiratory correction (4D-D), (c) 4D reconstruction with only cardiac gating (4D-C), and (d) 4D reconstruction from two near end-expiration bins (4D-R). The diaphragm motion magnitude was 2 cm and the anterior-posterior expansion of the chest was 1.2 cm.

E. Reconstructed NCAT Images

In Figure 7, we show a set of images reconstructed by 4D-D, 4D-C, and 4D-R from a typical noise realization. These images are shown for one short-axis and one long-axis slice of the LV in different cardiac gates (only every other gates are shown for brevity). The smoothing parameters used were $\beta_s = 0$ and $\beta_t = 0.001$ (based on optimal MSE results above). As can be seen, the LV wall in 4D-C (the inferior section in
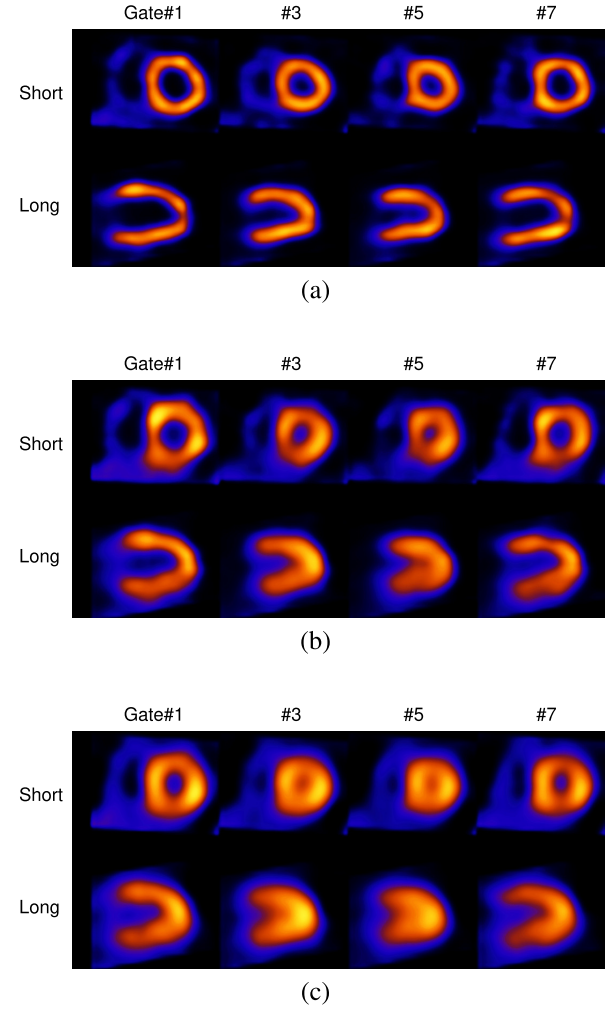
Fig. 8. Short axis and vertical-long axis slices of patient #1 by different methods: (a) proposed 4D reconstruction with dual cardiac-respiratory correction (4D-D), (b) 4D reconstruction with only cardiac gating (4D-C), and (c) clinical spatiotemporal reconstruction (ST121). The patient is interpreted as being normal, and the estimated peak-to-peak motion magnitude is 1.87 cm.

particular) suffers from distortion caused by respiratory blur; in comparison, the LV wall in 4D-D is noted to be improved among the different gates and is much closer to that of Ideal. Moreover, the LV in 4D-D (short-axis view) is also better separated from the nearby liver activity than in 4D-C. The images in 4D-R show high noise due to the much reduced counts with only two respiratory bins. However, the LV wall shape in 4D-R (short axis) is notably closer to that in 4D-D than 4D-C.

F. Clinical Reconstructions

In Figures 8 and 9, we show the reconstructed images for two patients (#1 and #2) by 4D-D, 4D-C, and ST121. For each subject, we show a short-axis and a long-axis slice of the LV in different cardiac gates. The following parameters were used in both 4D-D and 4D-C: $\beta_s = 0$ and $\beta_t = 0.001$, as in the NCAT data above.

From these results, the 4D-D images overall show an improved resolution of the LV wall over both 4D-C and
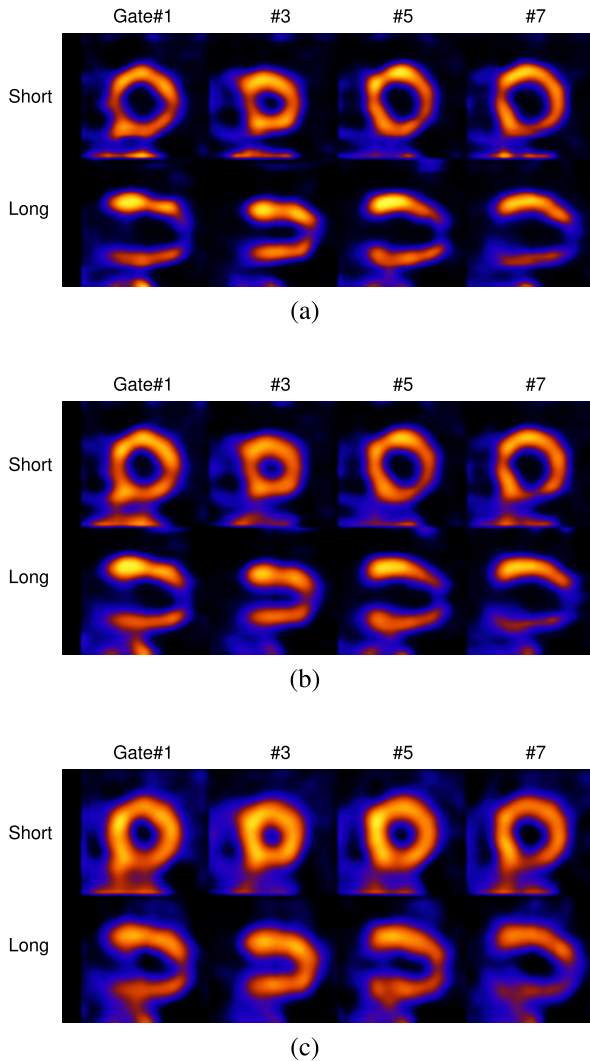
Fig. 9. Short axis and vertical-long axis slices of patient #2 by different methods: (a) proposed 4D reconstruction with dual cardiac-respiratory correction (4D-D), (b) 4D reconstruction with only cardiac gating (4D-C), and (c) clinical spatiotemporal reconstruction (ST121). The patient is interpreted as having an apical infarct, and the estimated peak-to-peak motion magnitude is 2.15 cm.

ST121 among all the subjects. The LV wall exhibits a higher contrast relative to the surrounding background in the 4D-D images. In addition, the blood pool in 4D-D suffers much less spill-over from the LV wall, particularly in gates near the end-systolic phase.

Quantitatively, we also computed the FWHM for a cross-section of the LV wall (as indicated in Figure 2). For patient #1 (Figure 8), the FWHM values are 1.84, 2.35 and 2.81 cm for 4D-D, 4D-C and ST121, respectively; similarly, for patient #2 (Figure 9), the FWHM values are 1.89, 2.25 and 2.71 cm for 4D-D, 4D-C and ST121, respectively. Similar improvements were also observed in the rest of the patients, but not shown here in the interest of space. Collectively, the obtained FWHM values in these patients are 2.02 ± 0.21 cm for 4D-D, 2.37 ± 0.22 cm for 4D-C, and 2.76 ± 0.22 cm for ST121.

Furthermore, it is observed from the clinical results that the reconstructed LV in 4D-D also reduces the effect of spill-over

from nearby activities in some subjects when they are present. For example, in Figure 9 (patient #2), the LV wall (short-axis) in 4D-D is well separated from some nearby bowel activity in gates #1 and #7, which is blended into the LV wall in both 4D-C and ST121 due to respiratory blur. Moreover, Figure 9 shows the reconstructed LV with a reported apical infarct. The perfusion defect is clearly seen in both 4D-C and 4D-D. The extent of the defect is noted to be better defined among all gates in 4D-D.

V. CONCLUSIONS

In this work, we developed a 4D reconstruction approach for suppressing the effect of respiratory motion in gated cardiac SPECT imaging. We first evaluated the proposed approach with a phantom simulation study, and compared it with 4D reconstruction with traditional cardiac gating. We then demonstrated the reconstruction approach on several sets of clinical acquisitions where the subjects exhibited different degrees of respiratory motion.

The simulated imaging results illustrate that, if only one respiratory interval was used for minimizing the motion blur, the reconstructed images would be too noisy to be useful due to the extremely low data counts. Compared with traditional cardiac gating (4D-C), using additional respiratory gating in 4D reconstruction (4D-D) can further improve the overall reconstruction accuracy (measured by MSE) of the myocardium, with the best MSE being reduced by as much as 22%. The bias in regional accuracy evaluation of the LV is much smaller in 4D-D than in 4D-C while achieving similar noise level. In addition, 4D-D could lead to improved lesion detection over 4D-C. In evaluation with clinical acquisitions, the 4D-D images from multiple patients show a better definition of the LV wall and blood pool compared with 4D-C and ST121 reconstructions. Moreover, 4D-D images can also correct spill-over effect from nearby activities into the myocardium.

In this work, we considered a translational motion model for respiratory motion correction. While simple, the results show that such a motion model could effectively improve the reconstruction accuracy in cardiac SPECT. Encouraged by these results, in the future we plan to further investigate whether it is beneficial by incorporating a more elaborate respiratory motion model.

Furthermore, in this work we quantified the lesion detectability in ED gate images. In practice, lesion detection is typically performed on ungated studies because of the high noise in gated images. But this is known to suffer from motion artifacts. Recent studies show that motion-compensated sum of gated images (called "motion-frozen" perfusion images) can improve the accuracy of gated myocardial perfusion SPECT in detection of coronary artery disease [42], [43]. The motion-frozen images are obtained from all the counts shifted to the ED gate. It is reasonable to expect that the improvement in individual gates can also lead to improvement in their motion-compensated sum. In the future it would be interesting to investigate how our proposed 4D reconstruction may improve the detectability in motion-frozen perfusion images.

REFERENCES

[1] J. A. Cooper, P. H. Neumann, and B. K. McCandless, "Effect of patient motion on tomographic myocardial perfusion imaging," *J. Nucl. Med.*, vol. 33, no. 8, pp. 1566–1571, 1992.

[2] E. G. DePuey and E. V. Garcia, "Updated imaging guidelines for nuclear cardiology procedures Part I," *J. Nucl. Cardiol.*, vol. 8, pp. G5–G58, Sep. 2001.

[3] M. A. King and T. R. Miller, "Use of a nonstationary temporal Wiener filter in nuclear medicine," *Eur. J. Nucl. Med.*, vol. 10, no. 9, pp. 458–461, 1985.

[4] D. S. Lalush and B. M. W. Tsui, "Block-iterative techniques for fast 4D reconstruction using *a priori* motion models in gated cardiac SPECT," *Phys. Med. Biol.*, vol. 43, pp. 875–886, Apr. 1998.

[5] D. R. Gilland, B. A. Mair, J. E. Bowsher, and J. Anderson, "Simultaneous reconstruction and motion estimation for gated cardiac ECT," in *Proc. IEEE Nucl. Sci. Symp. Conf. Rec.*, vol. 2. Apr. 2001, pp. 1069–1071.

[6] E. Gravier and Y. Yang, "Motion-compensated reconstruction of tomographic image sequences," in *Proc. IEEE Int. Conf. Image Process.*, vol. 2. Oct. 2003, pp. 807–810.

[7] M. Jin *et al.*, "A quantitative evaluation study of four-dimensional gated cardiac SPECT reconstruction," *Phys. Med. Biol.*, vol. 54, no. 18, pp. 5643–5659, 2009.

[8] W. Qi, Y. Yang, X. Niu, and M. A. King, "A quantitative study of motion estimation methods on 4D cardiac gated SPECT reconstruction," *Med. Phys.*, vol. 39, no. 8, pp. 5182–5194, 2012.

[9] M. Jin *et al.*, "4D reconstruction for low-dose cardiac gated SPECT," *Med. Phys.*, vol. 40, no. 2, p. 022501, 2013.

[10] W. Segars and B. M. W. Tsui, "Study of the efficacy of respiratory gating in myocardial SPECT using the new 4-D NCAT phantom," in *Proc. IEEE Nucl. Sci. Symp. Conf. Rec.*, vol. 3. Apr. 2001, pp. 1536–1539.

[11] D. Mitra, D. Eiland, M. Abdallah, R. Bouthcko, G. T. Gullberg, and N. Schechtmann, "SinoCor: Motion correction in SPECT," *Proc. SPIE*, vol. 8314, p. 831452, Feb. 2012.

[12] Y. Ueda, S. Kudomi, M. Koike, Y. Oishi, H. Iwanaga, and K. Ueda, "Correction of liver displacement due to irregular respiration for SPECT images obtained using a multiple short-time acquisition with breath-holding technique," *Radiol. Phys. Technol.*, vol. 5, no. 1, pp. 71–77, 2012.

[13] K. Cho, S. Kumiata, and T. Kumazaki, "Development of a respiratory gated myocardial SPECT system," *J. Nucl. Cardiol.*, vol. 6, pp. 20–28, Apr. 1999.

[14] G. J. Klein, B. W. Reutter, M. H. Ho, J. H. Reed, and R. H. Huesman, "Real-time system for respiratory-cardiac gating in positron tomography," *IEEE Trans. Nucl. Sci.*, vol. 45, no. 4, pp. 2139–2143, Aug. 1998.

[15] W. Lu, P. J. Parikh, J. P. Hubenschmidt, J. D. Bradley, and D. A. Low, "A comparison between amplitude sorting and phase-angle sorting using external respiratory measurement for 4D CT," *Med. Phys.*, vol. 33, no. 8, pp. 2964–2974, 2006.

[16] J. G. Parker, B. A. Mair, and D. R. Gilland, "Respiratory motion correction in gated cardiac SPECT using quaternion-based, rigid-body registration," *Med. Phys.*, vol. 36, pp. 4742–4754, Apr. 2009.

[17] W. Qi, Y. Yang, M. N. Wernick, P. H. Pretorius, and M. A. King, "Limited-angle effect compensation for respiratory binned cardiac SPECT," *Med. Phys.*, vol. 43, no. 1, pp. 443–454, 2016.

[18] J. Dey *et al.*, "Estimation and correction of cardiac respiratory motion in SPECT in the presence of limited angle effects due to irregular respiration," *Med. Phys.*, vol. 37, no. 12, pp. 6453–6465, 2010.

[19] C. Song, Y. Yang, M. N. Wernick, P. H. Pretorius, and M. A. King, "Optimizing motion correction in reconstruction of respiratory-gated SPECT," in *Proc. IEEE 13th Int. Symp. Biomed. Imag. (ISBI)*, Apr. 2016, pp. 36–39.

[20] G. Kovalski, Z. Keidar, A. Frenkel, J. Sachs, S. Attia, and H. Azhari, "Dual 'motion-frozen heart' combining respiration and contraction compensation in clinical myocardial perfusion SPECT imaging," *J. Nucl. Cardiol.*, vol. 16, no. 3, pp. 396–404, 2009.

[21] C. Chan *et al.*, "End-expiration respiratory gating for a high-resolution stationary cardiac SPECT system," *Phys. Med. Biol.*, vol. 59, pp. 6267–6287, Oct. 2014.

[22] W. Qi, Y. Yang, M. N. Wernick, and M. A. King, "4D reconstruction for dual cardiac-respiratory gated SPECT," in *Proc. IEEE Int. Conf. Image Process.*, Sep. 2013, pp. 2324–2328.

[23] F. Gigengack, L. Ruthotto, M. Burger, C. Wolters, X. Jiang, and K. Schafers, "Motion correction in dual gated cardiac PET using mass-preserving image registration," *IEEE Trans. Med. Imag.*, vol. 31, no. 3, pp. 698–712, Mar. 2012.

[24] S. Ambwani, S. Cho, W. Karl, A. Tawakol, and H. Pien, "A feasibility study of joint respiratory and cardiac motion correction for coronary PET/CT imaging," in *Proc. IEEE Int. Symp. Biomed. Imag. Nano Macro (ISBI)*, Apr. 2009, pp. 935–938.

[25] F. Buther *et al.*, "List mode-driven cardiac and respiratory gating in PET," *J. Nucl. Med.*, vol. 50, pp. 674–681, Apr. 2009.

[26] T.-S. Lee and B. M. W. Tsui, "The development and initial evaluation of a realistic simulated SPECT dataset with simultaneous respiratory and cardiac motion for gated myocardial perfusion SPECT," *Phys. Med. Biol.*, vol. 60, pp. 1399–1413, Feb. 2015.

[27] B. M. W. Tsui *et al.*, "Advances in 4D gated cardiac PET imaging for image quality improvement and cardiac motion and contractility estimation," in *Perspect. Nucl. Med. Mol. Diagnosis Integr. Therapy*, Y. Kuge, T. Shiga, and N. Tamaki, Eds. Japan: Springer, 2016, pp. 3–16.

[28] T. Feng, J. Wang, G. Fung, and B. Tsui, "Non-rigid dual respiratory and cardiac motion correction methods after, during, and before image reconstruction for 4D cardiac PET," *Phys. Med. Biol.*, vol. 61, no. 1, pp. 151–168, 2016.

[29] P. J. Slomka *et al.*, "Dual-gated motion-frozen cardiac PET with flurpiridaz F18," *J. Nucl. Med.*, vol. 56, no. 12, pp. 1876–1881, 2015.

[30] M. Teräs *et al.*, "Dual-gated cardiac PET—Clinical feasibility study," *Eur. J. Nucl. Med. Mol. Imag.*, vol. 37, no. 3, pp. 505–516, 2010.

[31] X. Niu, Y. Yang, M. N. Wernick, M. Jin, and M. A. King, "Effects of motion attenuation and scatter corrections on gated cardiac SPECT reconstruction," *Med. Phys.*, vol. 38, no. 12, pp. 6571–6585, 2011.

[32] S. Ahn and J. A. Fessler, "Globally convergent image reconstruction for emission tomography using relaxed ordered subsets algorithms," *IEEE Trans. Med. Imag.*, vol. 22, no. 5, pp. 613–626, May 2003.

[33] B. K. P. Horn and B. G. Schunck, "Determining optical flow," *Artif. Intell.*, vol. 17, nos. 1–3, pp. 185–203, Aug. 1981.

[34] W. Qi, Y. Yang, and M. King, "Effects of piecewise spatial smoothing in 4-D SPECT reconstruction," *IEEE Trans. Nucl. Sci.*, vol. 61, no. 1, pp. 182–191, Feb. 2014.

[35] W. P. Segars, "Development of a new dynamic NURBS-based cardiac-torso (NCAT) phantom," Ph.D. dissertation, Dept. Biomed. Eng., Univ. North Carolina, Chapel Hill, NC, USA, 2001.

[36] W. P. Segars and B. M. W. Tsui, "MCAT to XCAT: The evolution of 4-D computerized phantoms for imaging research," *Proc. IEEE*, vol. 97, no. 12, pp. 1954–1968, Dec. 2009.

[37] M. Ljungberg and S. V. Strand, "A Monte Carlo program simulating scintillation camera imaging," *Comput. Methods Prog. Biomed.*, vol. 29, no. 4, pp. 257–272, 1989.

[38] M. A. King, D. J. deVries, T.-S. Pan, P. H. Pretorius, and J. A. Case, "An investigation of the filtering of TEW scatter estimates used to compensate for scatter with ordered subset reconstruction," *IEEE Trans. Nucl. Sci.*, vol. 44, no. 3, pp. 1140–1145, Apr. 1997.

[39] H. M. Hudson and R. S. Larkin, "Accelerated image reconstruction using ordered subsets of projection data," *IEEE Trans. Nucl. Sci.*, vol. 13, no. 4, pp. 601–609, Apr. 1994.

[40] P. Pretorius, K. Johnson, and M. King, "Respiratory motion compensation in Tc-99m cardiac perfusion SPECT/CT stress acquisitions: Experience from 150+ patients," *J. Nucl. Med.*, vol. 55, p. 149, Apr. 2014.

[41] K. J. Myers and H. H. Barrett, "Addition of a channel mechanism to the ideal-observer model," *J. Opt. Soc. Amer. A*, vol. 4, no. 12, pp. 2447–2457, 1987.

[42] P. J. Slomka *et al.*, "'Motion-frozen' display and quantification of myocardial perfusion," *J. Nucl. Med.*, vol. 45, pp. 1128–1134, Apr. 2004.

[43] Y. Suzuki *et al.*, "'Motion-frozen myocardial perfusion SPECT improves detection of coronary artery disease in obese patients," *J. Nucl. Med.*, vol. 49, pp. 1075–1079, Oct. 2012.